JM PAPERS

Universal scaling law in turbulent Rayleigh–Bénard convection with and without roughness

Lyse Brichet[1] ⓘ, Nathan Carbonneau[2] ⓘ, Elian Bernard[1], Romane Braun[1], Lucas Méthivier[1] ⓘ, Yann Fraigneau[2], Didier Lucor[2], Francesca Chillà[1], Anne Sergent[2,3] ⓘ and Julien Salort[1] ⓘ

[1]CNRS, Laboratoire de physique, ENSL, Lyon F-69342, France
[2]Université Paris-Saclay, CNRS, LISN, Orsay F-91400, France
[3]Faculté des Sciences et Ingénierie, UFR d'Ingénierie, Sorbonne Université, Paris F-75005, France
Corresponding author: Julien Salort, julien.salort@ens-lyon.fr

Heat-transfer measurements published in the literature seem to be contradictory, some showing a transition for the dependance of the Nusselt number (Nu) with the Rayleigh number (Ra) behaviour at $Ra \approx 10^{11}$, some showing a delayed transition at higher Ra, or no transition at all. The physical origin of this discrepancy remains elusive, but is hypothesised to be a signature of the multiple possible flow configurations for a given set of control parameters, as well as the sub-critical nature of the transition to the ultimate regime (Roche 2020 *New J. Phys.* vol. 22, 073056; Lohse & Shishkina 2023 *Phys. Today* vol. 76, no. 11, 26–32). New experimental and numerical heat-flux and velocity measurements, both reaching Ra up to 10^{12}, are reported for a wide range of operating conditions, with either smooth boundaries, or mixed smooth–rough boundaries. Experiments are run in water at 40 °C (Prandtl number, Pr is 4.4), or fluorocarbon at 40 °C (Pr is 12), and aspect ratios 1 or 2. Numerical simulations implement the Boussinesq equations in a closed rectangular cavity with a Prandtl number 4.4, close to the experimental set-up, also with smooth boundaries, or mixed smooth–rough boundaries. In the new measurements in the rough part of the cell, the Nusselt number is compatible with a $Ra^{1/2}$ scaling (with logarithmic corrections), hinting at a purely inertial regime. In contrast to the Nu vs Ra relationship, we evidence that these seemingly different regimes can be reconciled: the heat flux, expressed as the flux Rayleigh number, $RaNu$, recovers a universal scaling with Reynolds number, which collapses all data, both our own and those in the literature, once a universal critical Reynolds number is exceeded. This universal collapse can be related

to the universal dissipation anomaly, observed in many turbulent flows (Dubrulle 2019 *J. Fluid Mech.* vol. 867, no. P1, 1).

Key words: Bénard convection, convection in cavities

1. Introduction

Turbulent Rayleigh-Bénard Convection is a model system where a layer of fluid is heated from below and cooled from above. It is controlled by three dimensionless parameters: the Rayleigh number Ra

$$Ra = \frac{g\alpha\Delta T H^3}{\nu\kappa}, \tag{1.1}$$

the Prandtl number Pr

$$Pr = \frac{\nu}{\kappa}, \tag{1.2}$$

and the aspect ratio $\Gamma = L/H$, where g is the acceleration due to gravity, α is the thermal expansion coefficient, ΔT is the temperature difference across the fluid layer, ν is the kinematic viscosity, κ is the thermal diffusivity, H is the height of the cell and L is the width of the cell. A long-standing endeavour consists of finding universal scaling laws for the heat transfer, expressed as the dimensionless parameter Nusselt number Nu (Chillà & Schumacher 2012; Stevens *et al.* 2013; Lohse & Shishkina 2023)

$$Nu = \frac{\dot{q}H}{\lambda\Delta T}, \tag{1.3}$$

where $\dot{q}$ is the heat flux, and λ is the thermal conductivity. This would allow the extrapolation of results from laboratory experiments to natural systems where highly turbulent natural convection plays a role. These include in particular convection in the ocean at the pole or in subglacial lakes (Couston & Siegert 2021), resulting in Rayleigh numbers beyond 10^{14}, and in the 'ultimate regime' of convection where $Nu \sim Ra^{1/2}$ (with logarithmic corrections) (Kraichnan 1962). However, experimental heat-transfer measurements published in the literature for $Ra > 10^{11}$ seem to be contradictory, some showing a transition at $Ra \approx 10^{11}$ (Chavanne *et al.* 1997; Niemela & Sreenivasan 2003a), some showing a delayed transition at higher Ra (He *et al.* 2012) or no transition at all (Niemela *et al.* 2000; Urban *et al.* 2019). These experiments are within Oberbeck–Boussinesq conditions (Roche *et al.* 2010) and share similar geometries, but differ in Prandtl numbers and details of the set-up. New recent theoretical models point out that the transition to the ultimate regime may be a subcritical process, and may depend on aspect ratio and Prandtl numbers (Roche 2020; Ahlers *et al.* 2022; Lohse & Shishkina 2023).

In this work, we evidence a way to recover universality. We report new velocity data obtained from shadowgraph imaging in parallelepiped Rayleigh–Bénard cells with or without roughness and using either deionised water or Fluorocarbon FC-770 as the working fluid, as well as new Direct Numerical Simulations (DNS), carried out in a similar geometric configuration filled with water. The Rayleigh numbers range between 5×10^8 and 3×10^{12}.

In these conditions, the flow is known to be able to reach various regimes and several possible scaling exponent for Nu versus Ra. This is a range of parameters where apparent disagreement is observed between the data from Grenoble, Oregon, Brno and Göttingen

cited above. And yet, we show that all the data, both from our new measurements and simulations, and from the literature, can be collapsed using the appropriate scaling of Reynolds and Prandtl numbers.

2. Experimental and numerical set-up

The cell dimensions are $41.5 \, \text{cm} \times 10.5 \, \text{cm} \times 41.5 \, \text{cm}$ for the aspect ratio 1 cell, and $41.5 \, \text{cm} \times 10.5 \, \text{cm} \times 20 \, \text{cm}$ for the aspect ratio 2 cell. The details of the cell are described in Méthivier *et al.* (2021). The Rayleigh number spans a wide range between 10^9 and 2.5×10^{12}, the Prandtl number between 4.3 and 7.0 in water and 11 and 14 in FC-770 and the aspect ratio is either 1 or 2. The experimental cells can be set up with roughness on the bottom plate, consisting in square roughness elements of height $h_0 = 2 \, \text{mm}$, machined in the plate, as described in Belkadi *et al.* (2020).

DNS are performed for two cavities at $Pr = 4.4$ (same as water), with depth to height aspect ratios $\Gamma^\star$ of one half and one quarter, and a width to height aspect ratio $\Gamma = 1$. Three surface states for the bottom wall have been modelled: smooth, rough with $h_0/H = 0.04$, rough with $h_0/H = 0.003$). (h_0/H is only for rough plates). Rayleigh numbers range from 5×10^8 to 10^{12}. The computational grids resolve the Kolmogorov scale in the whole domain, and follow the resolution criteria set in Shishkina *et al.* (2010). The simulation at $Ra = 10^{12}$ is performed on a $3328 \times 896 \times 5760$ grid. Statistical convergence of the integral heat-flux quantities is less than 2 %. Details of the numerical code, called SUNFLUIDH, can be found in Belkadi *et al.* (2021).

3. Heat-flux estimates

The experimental smooth cell (later referred to as 'SS') has entirely smooth boundaries, as described in Méthivier *et al.* (2021). For both experiments and DNS, in the rough case, the cell (later referred to as 'RS'), is asymmetrical, with a rough bottom plate and a smooth top plate.

As shown in our previous works (Tisserand *et al.* 2011; Rusaouen *et al.* 2018), this allows us to define Rayleigh and Nusselt numbers of the rough and smooth half-cells, provided the bulk temperature T_{bulk} is also known. The temperature drop across the boundary layer of the smooth plate, $\Delta T_s = T_{bulk} - T_{top}$, and the temperature drop across the boundary layer of the rough plate, $\Delta T_r = T_{bottom} - T_{bulk}$, allow us to estimate the total temperature difference across a corresponding virtual symmetric cell with identical smooth plates as $2\Delta T_s$, or with identical rough plates as $2\Delta T_r$, from which Ra_s, Nu_s, Ra_r, Nu_r are derived as

$$Ra_s = \frac{2g\alpha(T_{bulk} - T_{top})H^3}{\nu\kappa}, \tag{3.1}$$

$$Nu_s = \frac{\dot{q}H}{2\lambda(T_{bulk} - T_{top})}, \tag{3.2}$$

$$Ra_r = \frac{2g\alpha(T_{bottom} - T_{bulk})H^3}{\nu\kappa}, \tag{3.3}$$

$$Nu_r = \frac{\dot{q}H}{2\lambda(T_{bottom} - T_{bulk})}. \tag{3.4}$$

We have now operated the experimental rough configuration (RS) with Fluorocarbon FC-770, thus significantly extending the previous heat-transfer results in water
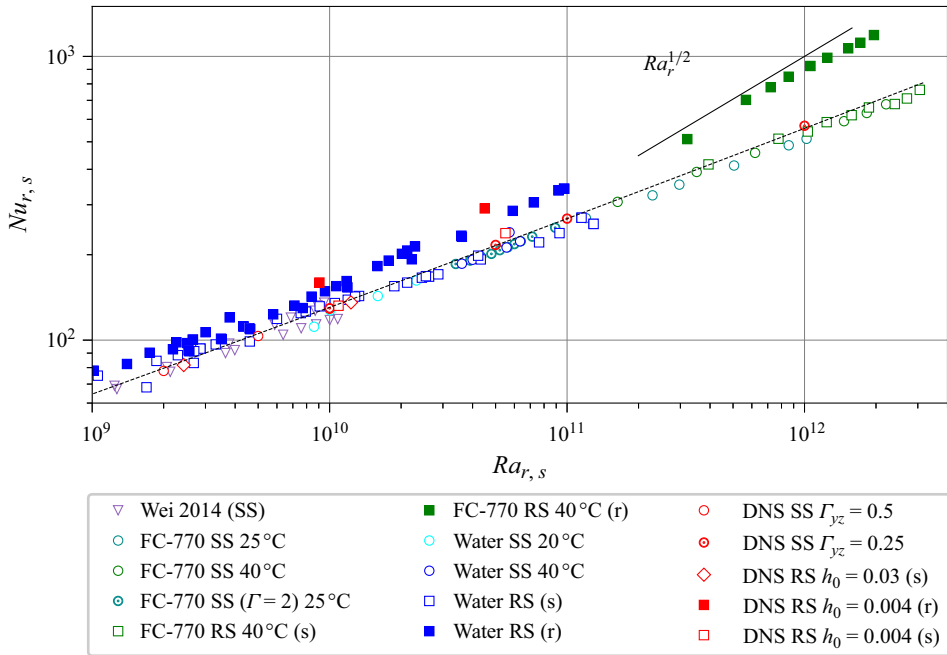
Figure 1. Heat-transfer measurements in experiments and in the numerical simulations. The RS cell in water from Salort *et al.* (2014). The SS cells in FC-770 from Méthivier *et al.* (2021). The SS cell in water, RS cell in FC-770 and DNS: new data. Solid black line: $Ra^{1/2}$. The effective exponent is closer to $Ra^{0.39}$ due to the logarithmic corrections. Purple down-pointing triangles: SS cell of Wei *et al.* (2014) (top and bottom half-cells). Dashed black line: Grossmann–Lohse model (Stevens *et al.* 2013).

(Salort *et al.* 2014). Figure 1 shows the new experimental data, as well as the new DNS data, compared with previous data. The Grossmann–Lohse model is also shown for comparison (with the prefactors from Stevens *et al.* 2013), as well as the experimental data of Wei *et al.* (2014) obtained in a symmetrical rough cell ('RR').

In the fluorocarbon cell, the thermal boundary layer, estimated as $\delta_{th} = H/(2Nu)$, ranges between 250 and 500 μm, much smaller than the roughness height h_0. The kinetic boundary layer, estimated as $\delta_v \approx \delta_{th} Pr^{1/3}$, ranges between 600 and 1100 μm, smaller than the roughness height h_0. Therefore, the rough cell lies in regime III as defined by Xie & Xia (2017). By the same definition, DNS configurations can be either in regime II or regime III. At $Ra = 10^{10}$, the simulation with the smaller roughness size ($h_0^\star = 0.003$) is in regime II (i.e. the thermal boundary layer is smaller than the roughness height h_0, whereas the kinetic one is larger), while the simulation with the larger roughness size ($h_0^\star = 0.04$) is in regime III. As the thickness of the thermal boundary layer decreases with the Rayleigh number, there is a threshold beyond which the roughness becomes active and induces an enhancement of heat transfer.

Even when the rough half-cell has a $Nu \sim Ra^{1/2}$ scaling (with logarithmic corrections), the Nusselt number in the smooth half-cell remains in good agreement, over more than 3 decades of Rayleigh number, with heat-transfer measurements in the SS cell, as well as with the Grossmann–Lohse model (Stevens *et al.* 2013). This shows that the top and bottom plates remain independent, even very far from the roughness-triggered enhancement threshold, and this holds even when the Nusselt number of the bottom half is nearly twice as large as that of the top half. This result is in agreement with our previous measurements

(Tisserand *et al.* 2011; Rusaouen *et al.* 2018), and extends them further from the roughness-enhanced transition. This is a major result that shows how the boundary layers adapt themselves to maintain the heat flux as a constant. It is different from the set-up of Wei *et al.* (2014) where asymmetry between top and bottom plates is observed, although this is also the case in their SS case.

4. Velocity estimates

In experiments, we computed the velocity fields using Correlation Image Velocimetry (CIV) on shadowgraph recordings in a wide range of *Ra* and *Pr*, in both for RS and SS cells, yielding consistent mean velocity and Reynolds number estimates for all configurations. The method consists in deriving velocity estimates from the shadowgraph pattern using the same algorithm we use for Particle Image Velocimetry (PIV) images, i.e. the image is divided into smaller boxes that are correlated at t and $t + \Delta t$, and the displacement that produces the maximum correlation is used as an estimate for the local velocity. In practice, we use a two-pass algorithm from FluidImage (Augier, Mohanan & Bonamy 2019) with initial box size 128 px × 128 px and a multipass zoom coefficient of 2, except for the RS FC-770 experiments which use an initial box size 64 px × 64 px.

Examples of raw shadowgraph patterns and mean velocity fields are shown in figures 2 and 3, for SS and RS cells. Using the shadowgraph image for CIV is possible at high *Ra*, because plumes fill the full cavity, and the correlation algorithm works everywhere. Plumes at the centre of the image are not visible on the raw shadowgraph because the contrast is much lower in the centre of the cell. However, we use a high-dynamics 14 bit camera, which allows us to resolve the plume pattern everywhere, including at the centre. Figure 4 shows a processed image for which the contrast limited adaptive histogram equalisation (CLAHE) method, implemented in the OpenCV Library Bradski (2000), has been applied. It is even more difficult to guess the mean flow pattern, but it clearly shows how homogeneous plume patterns actually are, once spatial variation of contrast is removed. The same holds even more for experiments in FC-770, but the patterns are so much smaller that they are difficult to render on a paper-sized figure.

This velocimetry method, based on the shadowgraph pattern, has previously been validated against standard PIV in experimental conditions where both were possible (Méthivier *et al.* 2021). One should be aware that the shadowgraph patterns result from the deviation of light across the cell depth. Therefore, the obtained velocity is integrated over the depth, in contrast to PIV which is computed on a plane.

In numerical simulations, slices at mid-plane are saved, allowing us to compute the mean velocity field at mid-depth, see figure 5. In both experiments and numerics, the large-scale Circulation (LSC) may go clockwise or anti-clockwise. To make comparison easier, we applied a mirror to the anti-clockwise fields before plotting, so that all fields appear clockwise. The DNS field at $Ra = 10^{10}$ is in good agreement with the PIV obtained previously (Liot *et al.* 2017).

The experimental estimates from CIV on the shadowgraph pattern are fairly similar to the mid-depth mean velocity estimates from the DNS, except in the bottom right and top left corners where the corner flows are highly three-dimensional: both rising and falling structures can be observed in the shadowgraph sequence, hence the CIV estimate tends to go to zero.

We find that the mean velocity field has the same structure at $Ra = 10^{10}$ and $Ra = 10^{12}$, and also does not change significantly in rough cells. The raw shadowgraph pictures show, however, stronger density gradients, and smaller structures, filling the cell further from the walls. Beyond $Ra = 10^{12}$, the shadowgraph pattern is much less inhomogeneous.
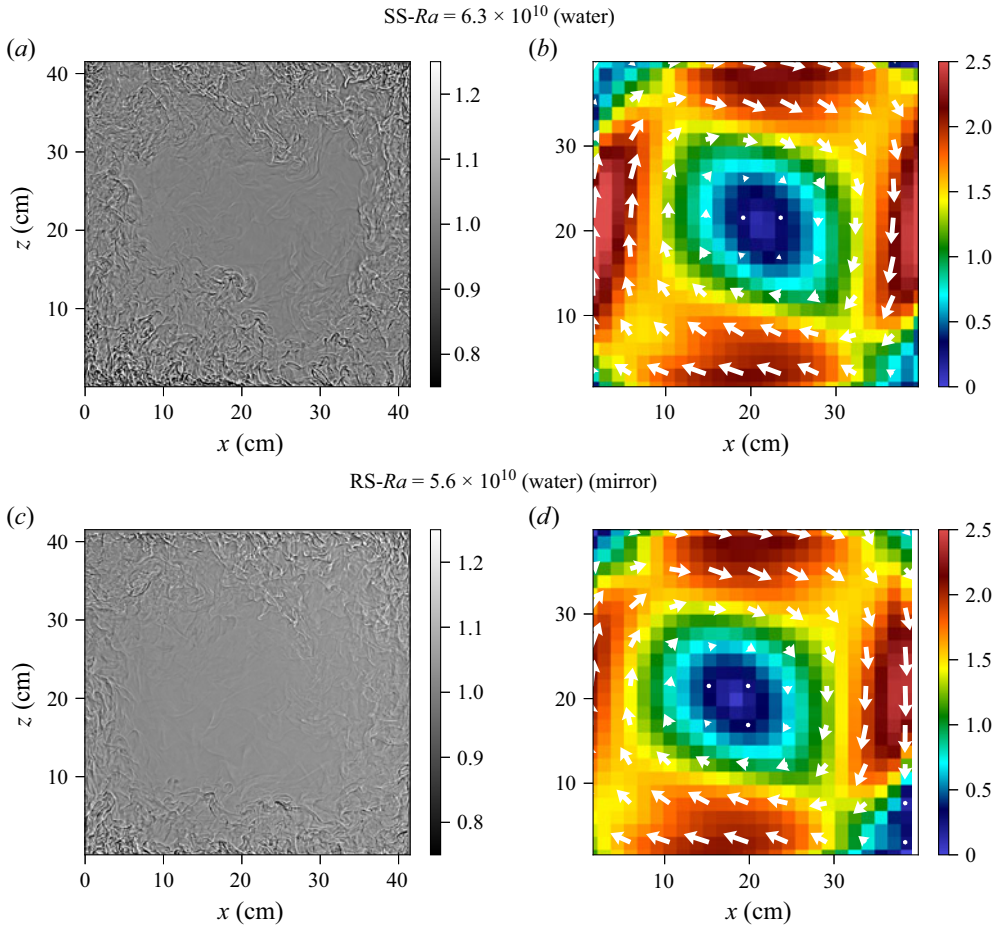
SS-$Ra = 6.3 \times 10^{10}$ (water)

RS-$Ra = 5.6 \times 10^{10}$ (water) (mirror)

Figure 2. Snapshots of experimental shadowgraph recordings (*a,c*), and mean velocity fields computed from CIV (*b,d*), in both SS and RS experimental configurations in water: SS water $Ra = 6.3 \times 10^{10}$, $Re = 1.6 \times 10^4$; RS water $Ra = 5.6 \times 10^{10}$, $Re = 1.4 \times 10^4$.

When roughness is added to the bottom plate, mean velocity is increased between 5 % and 20 % in the range of parameters explored in this work, but the overall structure of the mean flow is not significantly changed. However, it does not preclude stronger effects on the velocity fluctuations, as shown by Liot *et al.* (2017).

In the following, we focus on the velocity of the upwelling and downwelling jets to allow comparison with the literature where velocity is estimated with pairs of thermometers at mid-height (Wu & Libchaber 1992; Chavanne *et al.* 2001; Niemela *et al.* 2001; He *et al.* 2015; Musilová *et al.* 2017). To make the Reynolds number values quantitatively comparable, the values from Wei *et al.* (2014) have been corrected. Indeed, they defined their Reynolds numbers as

$$ Re = \frac{V_{osc} H}{\nu}, \qquad V_{osc} = \frac{4H}{\tau}, \tag{4.1} $$

where τ is an oscillation period computed from the autocorrelation of local thermistors. However, as shown by Niemela & Sreenivasan (2003*b*), the length of the roll is not $4H$ but $\alpha \cdot H$, where α is between 2 and 4, and strongly depends on Ra for $Ra < 10^{11}$. In the range

1025 A10-6

SS-$Ra = 1.7 \times 10^{12}$ (fc770) (mirror)
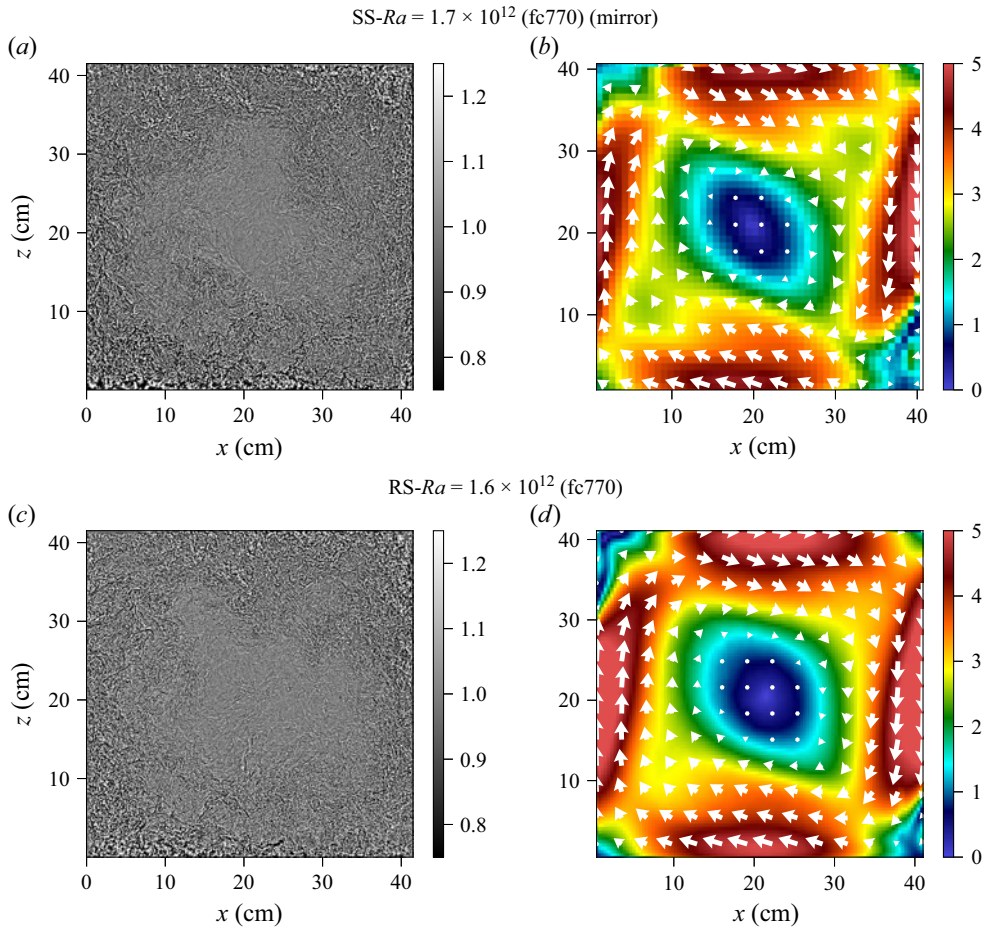

RS-$Ra = 1.6 \times 10^{12}$ (fc770)

Figure 3. Snapshots of experimental shadowgraph recordings (a,c), and mean velocity fields computed from CIV (b,d), in both SS and RS experimental configurations in FC-770: SS FC-770 $Ra = 1.7 \times 10^{12}$, $Re = 3.3 \times 10^4$; RS FC-770 $Ra = 1.6 \times 10^{12}$, $Re = 4.0 \times 10^4$.

of Rayleigh numbers of Wei *et al.* (2014), $\alpha \approx 3.4$, and therefore we apply a corrective prefactor 3.4/4.0 to their Reynolds numbers. With this correction, the Reynolds numbers of their SS cell collapse fairly well with those of the literature and of the present work. The Reynolds numbers of their rough cells are higher.

In symmetrical cells, we average the velocity of the downwelling and upwelling jets. In RS cells, we associate the downwelling jet with the top plate, and the upwelling jet with the bottom plate. Indeed, we use the following definition for the Reynolds numbers, $Re_{r,s}$, of the rough bottom and the smooth top:

$$Re_{r,s} = \frac{U_{up,down}H}{\nu}, \tag{4.2}$$

where $U_{up,down}$ is the maximum of the profile along x of vertical velocity in the plane at mid-height.

The Reynolds numbers in the various configurations, as well as those of the literature, show deviations of more than a factor 2, even when differences in the definition have been accounted for, see figure 6(a). These deviations, although relatively small, are significant
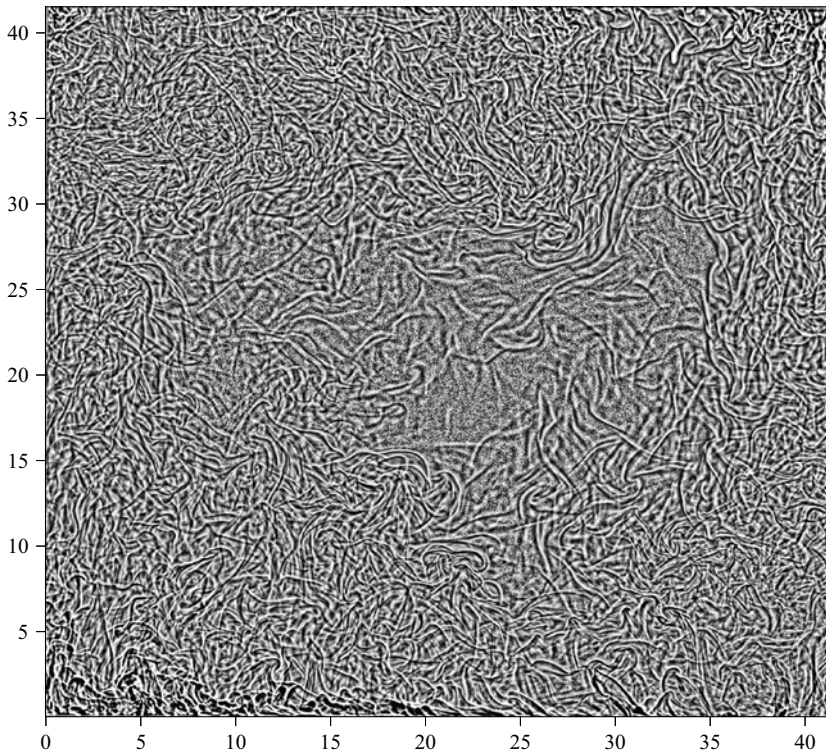
Figure 4. Snapshot of the experimental shadowgraph recording in the SS cell in water at $Ra = 6.3 \times 10^{10}$, after histogram equalisation with the CLAHE method. It is the same snapshot as in figure 2 (*a,c*), but allows us to visualise that plumes fill the full cavity and the pattern is almost homogeneous, once the inhomogeneity of contrast has been removed.

for quantities that scale with a power of the Reynolds number. For example, the Reynolds number in the RS cell using fluorocarbon is larger than in the SS case, and additionally is asymmetric (velocity is larger near the rough plate). This Reynolds number enhancement triggered by roughness was not visible in our previous measurements using PIV in water at lower Prandtl and Rayleigh numbers (Liot *et al.* 2017). Indeed, the Rayleigh number of the new data obtained in fluorocarbon is a decade larger and further from the threshold where roughness-enhanced heat transfer is triggered (regime II) than the rough cell using water. This is also observed in the DNS results. The higher Prandtl number also further separates the thermal and viscous boundary layers, which probably plays a role in the boundary layer response to plate roughness.

5. Discussion

One interesting quantity is the friction coefficient

$$\frac{RaNu}{Re^3Pr^2},$$
(5.1)

which was used by Chavanne *et al.* as an indicator of the transition to turbulence in the boundary layers (Chavanne *et al.* 2001), and can alternatively be interpreted as proportional to the ratio, $\mathcal{R}_\epsilon$, between the kinetic energy dissipation rate ϵ and the contribution of the bulk in kinetic energy dissipation rate $\epsilon_{u,bulk}$ (Grossmann & Lohse 2000)
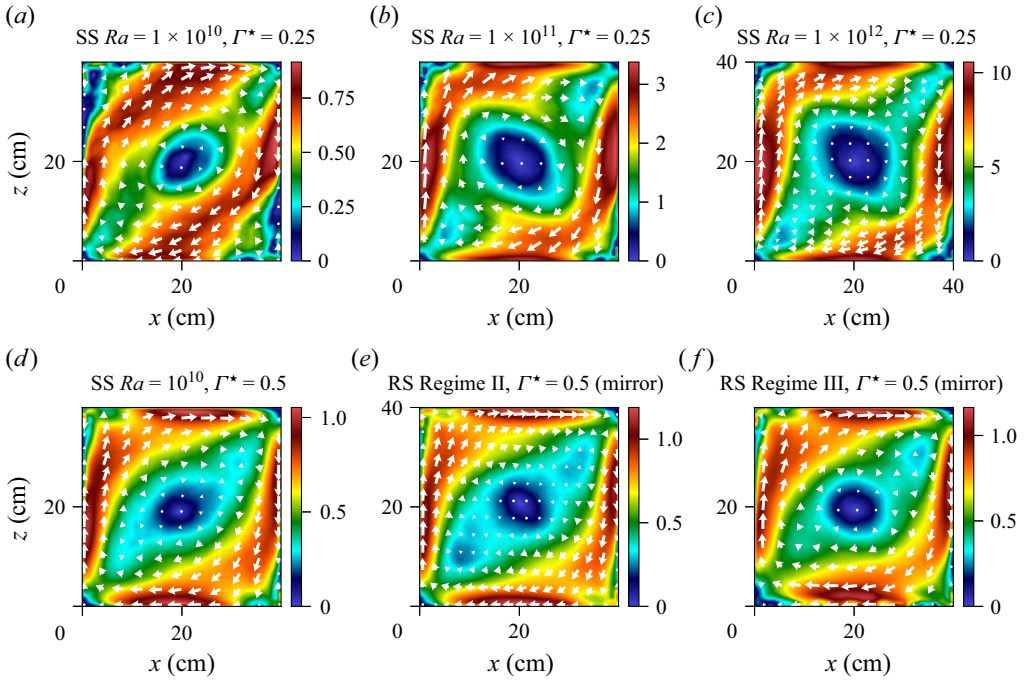
Figure 5. Mean velocity fields from the DNS at mid-depth for both depth to height aspect ratios $\Gamma^\star$ (see text, § 2). (*a–c*) Rayleigh number dependence. (*d–f*) comparison SS vs RS.

$$\epsilon = \frac{\nu^3}{H^4}(Nu - 1)RaPr^{-2} = \epsilon_{u,BL} + \epsilon_{u,bulk}, \tag{5.2}$$

and in the case of a turbulent bulk

$$\epsilon_{u,bulk} \propto \frac{\nu^3}{H^4}Re^3. \tag{5.3}$$

Hence, in the turbulent regime,

$$\mathcal{R}_\epsilon = \frac{\epsilon}{\epsilon_{u,bulk}} \sim \frac{NuRaPr^{-2}}{Re^3}. \tag{5.4}$$

In the range of parameters explored in this work, we evidence a transition at a critical Reynolds number, $Re_c \approx 10^4$. Beyond this transition, the friction coefficient no longer depends on the Reynolds number, or does so only very weakly, see figure 6(*b*). In the DNS, the ratio $\mathcal{R}_\epsilon = \epsilon/\epsilon_{u,bulk}$ can be estimated directly from the three-dimensional velocity fields using the local definition of ϵ

$$\epsilon(\boldsymbol{x}, t) = \frac{\nu}{2}\sum_{i=1}^{3}\sum_{j=1}^{3}\left(\partial_j u_i + \partial_i u_j\right)^2, \tag{5.5}$$

$$\epsilon = \frac{1}{V}\int_V \langle\epsilon(\boldsymbol{x}, t)\rangle_t \, d^3\boldsymbol{x}, \tag{5.6}$$

$$\epsilon_{u,bulk} = \frac{1}{V}\int_{V_{bulk}} \langle\epsilon(\boldsymbol{x}, t)\rangle_t \, d^3\boldsymbol{x}, \tag{5.7}$$
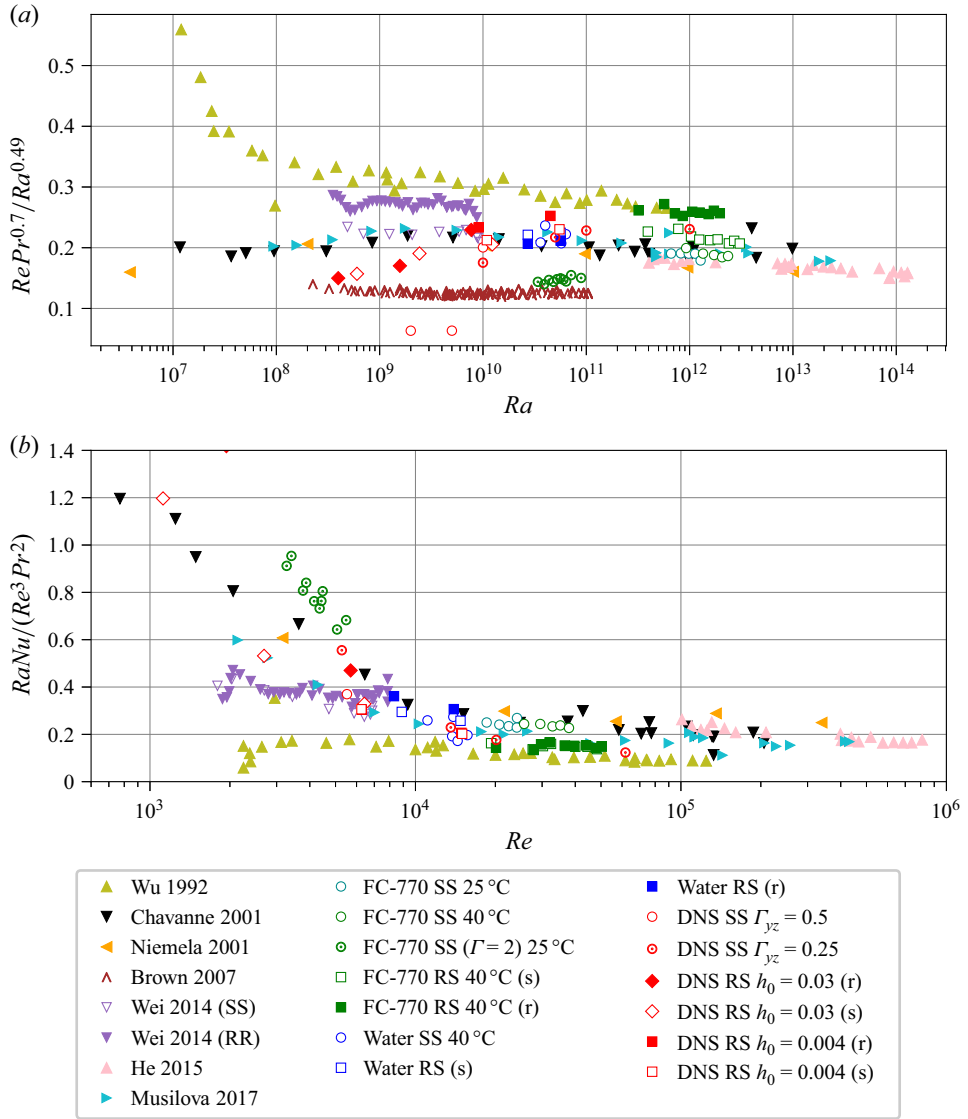
Figure 6. (*a*) Reynolds number measurements in FC-770 (green), water (blue) and from DNS (red), in RS (squares) and SS (circles) cells. Data from Wu & Libchaber (1992), Chavanne *et al.* (2001), Niemela *et al.* (2001), Brown, Funfschilling & Ahlers (2007), Wei *et al.* (2014), He *et al.* (2015) and Musilová *et al.* (2017) are plotted for comparison (triangles). A corrective factor has been applied to the Reynolds numbers of Wei *et al.* (2014) (see text). (*b*) Friction coefficient for all data points (same symbols). The heat flux, $RaNu$, collapses for all data with $RaNu \sim 0.2Re^3Pr^2$.

where $V = \Gamma\Gamma^\star H^3$ is the volume of the convection cell and V_{bulk} is the volume of the bulk.

The actual value of the ratio $\mathcal{R}_\epsilon$ depends on the definition of the bulk region. In the following estimates, we use a practical definition based on the efficiency of mixing in the turbulent bulk: we define the bulk as the region where the mean temperature gradient vanishes (in practice $\partial_z\theta < 10^{-3}$). Indeed, in the turbulent bulk, mixing makes the mean temperature homogeneous.
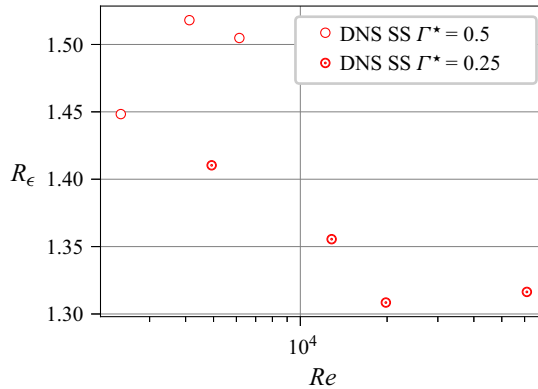
1025 A10-10

Figure 7. Inverse of the bulk fraction of kinetic dissipation, R_ϵ, in the DNS estimated from the three-dimensional velocity gradients (see text).

The values are shown in figure 7. The plot is similar to that in figure 6(*b*). The value at the highest *Re* when the plateau is reached, of order $\mathcal{R}_\epsilon \sim 1.3$, suggests that more than 75 % of the kinetic dissipation occurs outside the boundary layers, and confirms that the total dissipation is dominated by the turbulent bulk.

This transition may correspond to the mixing transition in fully developed turbulent flows described by Dimotakis (2000), which is thought to occur for an outer-scale Reynolds number of order 10^4 (or R_λ of order 10^2). In his paper, he suggested that this mixing transition coincides with the soft turbulence –hard turbulence transition predicted by Castaing *et al.* (1989) in turbulent thermal convection. In their original paper, Castaing *et al.* (1989) claimed that they observed the soft–hard transition at a lower Rayleigh number of order 4×10^7, based on the observation of a change in the temperature fluctuation distribution (Heslot, Castaing & Libchaber 1987), which was later found to not be a good proxy. We propose that the hard turbulence regime, which corresponds to the mixing transition, is actually reached at higher Reynolds numbers, when the friction coefficient reaches a plateau.

More generally, this plateau is a signature of the dissipation anomaly in turbulence (Dubrulle 2019), which was also observed numerically by Pandey *et al.* (2022) in turbulent Rayleigh–Bénard convection, and has been observed in various turbulent systems, such as grid flows where it occurs at $R_\lambda \sim 50$ (Sreenivasan 1984), or von Kármán flows where estimates based on torque measurements yields a transition at $Re \sim 300$ (Saint-Michel *et al.* 2014). Our results show that the plateau is very robust and consistent with both numerical and experimental observations in turbulent Rayleigh–Bénard convection, as well as previous results in the literature.

The bulk of Rayleigh–Bénard convection in this range of forcing is completely determined by turbulent mixing, regardless of whether or not the Nusselt versus Rayleigh number relationship shows a change in their scaling relationship. Note that, while the critical Reynolds number appears to be universal, as well as the plateau in the turbulent regime, the path towards turbulence does not have to be unique, as noted by Dimotakis (2000). While the data for $Re < Re_c$ reveal some non-universality, the important point is that all the data collapse beyond Re_c.

Therefore, we get a relationship between the dimensionless heat flux, $RaNu$, and the Reynolds and Prandtl numbers, where

$$RaNu = \frac{g\rho^2 \alpha c_p H^4}{\mu \lambda^2} \dot{q}, \qquad (5.8)$$

where ρ is the density, c_p is the specific heat capacity and $\mu = \rho\nu$ is the dynamical viscosity. The phenomenological relationship is

$$RaNu \approx 0.2Re^3Pr^2. \tag{5.9}$$

While this scaling has been reported previously for individual sets of experiments (Chavanne *et al.* 2001; Musilová *et al.* 2017), the main result of this work is that the prefactor is universal, and does not change when the *Nu* vs *Ra* scaling law is changed, either by roughness or by the transition to the ultimate regime, hence collapsing data from experiments thought to be in quantitative disagreement.

Indeed, it is remarkable that this relationship, (5.9), holds for the Grenoble data which evidence a transition to the ultimate regime, as well as data which do not evidence such a transition, and also in the case of rough cells in which $Nu \sim Ra^{1/2}$, as well as smooth cells with a classical scaling. This shows that all these experiments lie in the turbulent regime, nevertheless, at moderate Prandtl numbers, $Nu(Ra)$ it is not unique because the Nusselt number depends on ϵ_θ, which in these regimes depends on the local form of the thermal boundary layer which has certainly a strong interaction with LSC but also depends on boundary details. Although this should not be a surprise, as theories need to set both ϵ and ϵ_θ to make a prediction on the Nusselt number (Kraichnan 1962; Castaing *et al.* 1989; Shraiman & Siggia 1990; Grossmann & Lohse 2000, 2011), the critical shear Reynolds number is often brought up as a control parameter for the onset of the ultimate regime (Stevens *et al.* 2013; Lohse & Shishkina 2023).

The present result shows that this may not be the discriminating criterion to understand why several datasets in the literature do not evidence a transition, or evidence a delayed one. Indeed, all these high-*Ra* seemingly conflicting datasets already lie beyond the transition to turbulence where the kinetic dissipation rate scales like Re^3. The condition on the Reynolds is therefore fulfilled. It appears, however, that this is not sufficient.

In this work, we have used the outer Reynolds number as a proxy, while it would be more physically appropriate to use R_λ. The reason is that we do not have access to R_λ for most of the data discussed in this paper. However, since the outer Reynolds number is determined by the wind, and the Reynolds number is not the discriminating factor to understand the difference between experiments which evidence the ultimate regime and those that do not, it follows that the mean wind is not the limiting factor for the onset of the ultimate regime in these experiments.

This is consistent with previous works: (i) the onset of the transition to the ultimate regime in Grenoble is not modified when the mean wind is changed (Roche *et al.* 2010), (ii) the velocity profiles have a logarithmic profile even at relatively low Rayleigh numbers (Liot *et al.* 2016*a,b*) in the classical regime and (iii) the influence of the mean wind intensity on the global heat transport is very weak (Ciliberto, Cioni & Laroche 1996; Ahlers, Grossmann & Lohse 2009), even when the wind is highly depleted (Carbonneau *et al.* 2025), suggesting that a Reynolds number based on fluctuations would be more relevant than one based on the mean wind, in agreement with Roche (2020).

Declaration of interests. The authors report no conflict of interest.

<div align="center">REFERENCES</div>

AHLERS, G. *et al.* 2022 Aspect ratio dependence of heat transfer in a cylindrical Rayleigh–Bénard cell. *Phys. Rev. Lett.* **128**, 084501.

AHLERS, G., GROSSMANN, S. & LOHSE, D. 2009 Heat transfer and large scale dynamics in turbulent Rayleigh–Bénard convection. *Rev. Mod. Phys.* **81** (2), 503–537.

AUGIER, P., MOHANAN, A.V. & BONAMY, C. 2019 Fluiddyn: a Python open-source framework for research and teaching in fluid dynamics by simulations, experiments and data processing. *J. Open Res. Softw.* **7**, 9.

BELKADI, M., GUISLAIN, L., SERGENT, A., PODVIN, B., CHILLÀ, F. & SALORT, J. 2020 Experimental and numerical shadowgraph in turbulent Rayleigh–Bénard convection with a rough boundary: investigation of plumes. *J. Fluid Mech.* **895**, A7.

BELKADI, M., SERGENT, A., FRAIGNEAU, Y. & PODVIN, B. 2021 On the role of roughness valleys in turbulent Rayleigh–Bénard convection. *J. Fluid Mech.* **923**, A6.

BRADSKI, G. 2000 The OpenCV library. *Dr. Dobb's J. Softw. Tools* **25** (11), 122–125.

BROWN, E., FUNFSCHILLING, D. & AHLERS, G. 2007 Anomalous Reynolds-number scaling in turbulent Rayleigh–Bénard convection. *J. Stat. Mech.* **2007**, P10005.

CARBONNEAU, N., SALORT, J., FRAIGNEAU, Y. & SERGENT, A. 2025 Influence of wind on heat transfer in turbulent convection with roughness. In *33e Congrès de la Société Française de Thermique*. https://doi.org/10.25855/SFT2025-112

CASTAING, B., GUNARATNE, G., HESLOT, F., KADANOFF, L., LIBCHABER, A., THOMAE, S., WU, X., ZALESKI, S. & ZANETTI, G. 1989 Scaling of hard thermal turbulence in Rayleigh–Bénard convection. *J. Fluid Mech.* **204**, 1–30.

CHAVANNE, X., CHILLÀ, F., CASTAING, B., HÉBRAL, B., CHABAUD, B. & CHAUSSY, J. 1997 Observation of the ultimate regime in Rayleigh–Bénard convection. *Phys. Rev. Lett.* **79**, 3648–3651.

CHAVANNE, X., CHILLÀ, F., CHABAUD, B., CASTAING, B. & HÉBRAL, B. 2001 Turbulent Rayleigh–Bénard convection in gaseous and liquid He. *Phys. Fluids* **13** (5), 1300–1320.

CHILLÀ, F. & SCHUMACHER, J. 2012 New perspectives in turbulent Rayleigh–Bénard convection. *Eur. Phys. J. E* **35**, 58.

CILIBERTO, S., CIONI, S. & LAROCHE, C. 1996 Large-scale flow properties of turbulent thermal convection. *Phys. Rev. E* **54** (6), R5901–R5904.

COUSTON, L.-A. & SIEGERT, M. 2021 Dynamic flows create potentially habitable conditions in Antarctic subglacial lakes. *Sci. Adv.* **7** (8), eabc3972.

DIMOTAKIS, P.E. 2000 The mixing transition in turbulent flows. *J. Fluid Mech.* **409**, 69–98.

DUBRULLE, B. 2019 Beyond Kolmogorov cascades. *J. Fluid Mech.* **867** (P1), 1.

GROSSMANN, S. & LOHSE, D. 2000 Scaling in thermal convection: a unifying theory. *J. Fluid Mech.* **407**, 27–56.

GROSSMANN, S. & LOHSE, D. 2011 Multiple scaling in the ultimate regime of thermal convection. *Phys. Fluids* **23**, 045108.

HE, X., FUNFSCHILLING, D., BODENSCHATZ, E. & AHLERS, G. 2012 Heat transport by turbulent Rayleigh–Bénard convection for $Pr \simeq 0.8$ and $4 \times 10^{11} < Ra < 2 \times 10^{14}$: ultimate-state transition for aspect ratio $\gamma = 1.00$. *New J. Phys.* **14**, 063030.

HE, X., VAN GILS, D.P.M., BODENSCHATZ, E. & AHLERS, G. 2015 Reynolds numbers and the elliptic approximation near the ultimate state of turbulent Rayleigh–Bénard convection. *New J. Phys.* **17**, 063028.

HESLOT, F., CASTAING, B. & LIBCHABER, A. 1987 Transitions to turbulence in Helium gas. *Phys. Rev. A* **36** (12), 5870–5873.

KRAICHNAN, R.H. 1962 Turbulent thermal convection at arbitrary Prandtl number. *Phys. Fluids* **5** (11), 1374–1389.

LIOT, O., EHLINGER, Q., RUSAOUËN, E., COUDARCHET, T., SALORT, J. & CHILLÀ, F. 2017 Velocity fluctuations and boundary layer structure in a rough Rayleigh–Bénard cell filled with water. *Phys. Rev. Fluids* **2**, 044605.

LIOT, O., GAY, A., SALORT, J., BOURGOIN, M. & CHILLÀ, F. 2016a Inhomogeneity and Lagrangian unsteadiness in turbulent thermal convection. *Phys. Rev. Fluids* **1**, 064406.

LIOT, O., SALORT, J., KAISER, R., DU PUITS, R. & CHILLÀ, F. 2016b Boundary layer structure in a rough Rayleigh–Bénard cell filled with air. *J. Fluid Mech.* **786**, 275–293.

LOHSE, D. & SHISHKINA, O. 2023 Ultimate turbulent thermal convection. *Phys. Today* **76** (11), 26–32.

MUSILOVÁ, V., KRÁLIK, T., MANTIA, M.La, MACEK, M., URBAN, P. & SKRBEK, L. 2017 Reynolds number scaling in cryogenic turbulent Rayleigh–Bénard convection in a cylindrical aspect ratio one cell. *J. Fluid Mech.* **832**, 721–744.

MÉTHIVIER, L., BRAUN, R., CHILLÀ, F. & SALORT, J. 2021 Turbulent transition in Rayleigh–Bénard convection with fluorocarbon. *Europhys. Lett.* **136**, 10003.

NIEMELA, J.J., SKRBEK, L., SREENIVASAN, K.R. & DONNELLY, R.J. 2000 Turbulent convection at very high Rayleigh numbers. *Nature* **404**, 837–840.

NIEMELA, J.J., SKRBEK, L., SREENIVASAN, K.R. & DONNELLY, R.J. 2001 The wind in confined thermal convection. *J. Fluid Mech.* **449**, 169–178.

NIEMELA, J.J. & SREENIVASAN, K.R. 2003a Confined turbulent convection. *J. Fluid Mech.* **481**, 355–384.

NIEMELA, J.J. & SREENIVASAN, K.R. 2003b Rayleigh-number evolution of large-scale coherent motion in turbulent convection. *Europhys. Lett.* **62**, 829–833.

PANDEY, A., KRASNOV, D., SREENIVASAN, K.R. & SCHUMACHER, J. 2022 Convective mesoscale turbulence at very low Prandtl numbers. *J. Fluid Mech.* **948**, A23.

QUEMENER, E. & CORVELLEC, M. 2013 Sidus—the solution for extreme deduplication of an operating system. *Linux J.* **2013** (235), 3.

ROCHE, P.-E. 2020 The ultimate state of convection: a unifying picture of very high Rayleigh numbers experiments. *New J. Phys.* **22**, 073056.

ROCHE, P.-E., GAUTHIER, F., KAISER, R. & SALORT, J. 2010 On the triggering of the ultimate regime of convection. *New J. Phys.* **12**, 085014.

RUSAOUEN, E., LIOT, O., SALORT, J., CASTAING, B. & CHILLÀ, F. 2018 Thermal transfer in Rayleigh–Bénard cell with smooth or rough boundaries. *J. Fluid Mech.* **837**, 443–460.

SAINT-MICHEL, B. *et al.* 2014 Probing quantum and classical turbulence analogy in von Kármán liquid helium, nitrogen, and water experiments. *Phys. Fluids* **26**, 125109.

SALORT, J., LIOT, O., RUSAOUEN, E., SEYCHELLES, F., TISSERAND, J.-C., CREYSSELS, M., CASTAING, B. & CHILLÀ, F. 2014 Thermal boundary layer near roughnesses in turbulent Rayleigh–Bénard convection: flow structure and multistability. *Phys. Fluids* **26**, 015112.

SHISHKINA, O., STEVENS, R.J.A.M., GROSSMANN, S. & LOHSE, D. 2010 Boundary layer structure in turbulent thermal convection and its consequences for the required numerical resolution. *New J. Phys.* **12**, 075022.

SHRAIMAN, B.I. & SIGGIA, E.D. 1990 Heat transport in high-Rayleigh-number convection. *Phys. Rev. A* **42** (6), 3650–3653.

SREENIVASAN, K.R. 1984 On the scaling of the turbulence energy dissipation rate. *Phys. Fluids* **27** (5), 1048.

STEVENS, R.J.A.M., VAN DER POEL, E.P., GROSSMANN, S. & LOHSE, D. 2013 The unifying theory of scaling in thermal convection: the updated prefactors. *J. Fluid Mech.* **730**, 295–308.

TISSERAND, J.-C., CREYSSELS, M., GASTEUIL, Y., PABIOU, H., GIBERT, M., CASTAING, B. & CHILLÀ, F. 2011 Comparison between rough and smooth plates within the same Rayleigh–Bénard cell. *Phys. Fluids* **23**, 015105.

URBAN, P., HANZELKA, P., KRÁLIK, T., MACEK, M. & MUSILOVÁ, V. 2019 Elusive transition to the ultimate regime of turbulent Rayleigh–Bénard convection. *Phys. Rev. E* **99**, 011101(R).

WEI, P., CHAN, T.-S., NI, R., ZHAO, X.-Z. & XIA, K.-Q. 2014 Heat transport properties of plates with smooth and rough surfaces in turbulent thermal convection. *J. Fluid Mech.* **740**, 28–46.

WU, X.-Z. & LIBCHABER, A. 1992 Scaling relations in thermal turbulence: the aspect-ratio dependence. *Phys. Rev. A* **45** (2), 842–845.

XIE, Y.-C. & XIA, K.-Q. 2017 Turbulent thermal convection over rough plates with varying roughness geometries. *J. Fluid Mech.* **825**, 573–599.